Adult-neurogenesis allows for representational stability and flexibility in early olfactory system

Zhen Chen [1], Krishnan Padmanabhan [2]

1. Department of Brain and Cognitive Sciences, University of Rochester, Rochester, NY 14627;

2. Department of Neuroscience, University of Rochester School of Medicine and Dentistry, Rochester, NY 14642.

* Krishnan Padmanabhan

Email: Krishnan_Padmanabhan@urmc.rochester.edu

Zhen Chen: ORCID iD: https://orcid.org/0000-0002-5590-3552

Krishnan Padmanabhan: ORCID iD: https://orcid.org/0000-0002-3255-8346

Abstract

In the early olfactory system, adult-neurogenesis, a process of neuronal replacement results in the continuous reorganization of synaptic connections and network architecture throughout the animal's life. This poses a critical challenge: How does the olfactory system maintain stable representations of odors and therefore allow for stable sensory perceptions amidst this ongoing circuit instability? Utilizing a detailed spiking network model of early olfactory circuits, we uncovered dual roles for adult-neurogenesis: one that both supports representational stability to faithfully encode odor information and also one that facilitates plasticity to allow for learning and adaptation. In the main olfactory bulb, adult-neurogenesis affects neural codes in individual mitral and tufted cells but preserves odor representations at the neuronal population level. By contrast, in the olfactory piriform cortex, both individual cell responses and overall population dynamics undergo progressive changes due to adult-neurogenesis. This leads to representational drift, a gradual alteration in sensory perception. Both processes are dynamic and depend on experience such that repeated exposure to specific odors reduces the drift due to adult-neurogenesis; thus, when the odor environment is stable over the course of adult-neurogenesis, it is neurogenesis that actually allows the representations to remain stable in piriform cortex; when those olfactory environments change, adult-neurogenesis allows the cortical representations to track environmental change. Whereas perceptual stability and plasticity due to learning are often thought of as two distinct, often contradictory processing in neuronal coding, we find that adult-neurogenesis serves as a shared mechanism for both. In this regard, adult-neurogenesis in the mammalian olfactory bulb that has been the focus of considerable study in chemosensory neuroscience may be the mechanistic underpinning behind an array of complex computations.

Introduction

In the rodent brain, the main olfactory bulb (MOB) is one of two regions where neurogenesis persists throughout the animal's lifetime [1]. Adult-born cells in the sub-ventricular zone migrate to the MOB, where nearly 95% differentiate into inhibitory adult-born granule cells (abGCs) forming reciprocal dendro-dendritic connections [2,3] with the principal excitatory cells of the MOB, the mitral and tufted (M/T) cells. M/T cells in turn relay the chemosensory information to the downstream targets including the olfactory or piriform cortex (PCx) [4–6]. Although both the cellular composition and synaptic organization of this circuit undergo constant changes due to adult-neurogenesis [7], animals are nonetheless able to perform incredibly complex behavioral tasks related to the determination of odor identity and concentration, suggesting that they maintain stable representations of odors. This raises two critical questions: Does the encoding of odors via patterns of neural activity throughout the early olfactory system undergo changes as a result of this ongoing plasticity, and if so, how? If changes in neural activity due to adult-neurogenesis percolate throughout early olfactory circuits, what computational principles allow the system to represent the same odor stably over time?

Previous studies have primarily explored the plasticity at synapses between M/T cells and abGCs, particularly in relation to olfactory learning [8–10]. It is known that sensory experience influences the survival and synaptic turnover of abGCs with M/T cells [7,11], impacting both the normal activity of these cells [12] and animal's performance in odor discrimination tasks [13]. However, the implications of these local synaptic changes in the bulb on the downstream areas, including in the PCx, which is critical for olfactory perception and learning [14,15], remain largely unexplored.

The three-layer PCx is thought to be a region where the components of an odor are assembled into an olfactory percept or representation. Subsets of piriform cells (PCs) respond when multiple M/T cells are activated in complex temporal sequences [16–18]. A given population of M/T cells from a single glomerulus, a neuropil like structure where inputs from individual olfactory receptor neuron types converge [19,20], project randomly to a distributed array of PCs [4–6]. As odor information in PCx is coded for through the combinatorial activity of PCs [21,22] it is hypothesized that PCx is where stable representations of odors are maintained [23]. However, recent evidence is beginning to challenge this idea [24]. First, NMDA mediated long-term potentiation (LTP) in both afferent and associate fibers to PCx [25,26] is similar to that observed in the CA1 region of hippocampus. PCs thus undergo synaptic plasticity on scales observed in other regions where representations are not stable [27]. Second, recent studies examining the responses of PCs over months demonstrate that patterns of activity in both individual cells and populations of cells can drift over time [24]. This representational drift has led to the hypothesis that PCx, rather than being a primary sensory area, may be more like an association cortical region. However, the mechanisms by which this drift in PCx occurs remain unknown.

One clue that adult-neurogenesis in MOB may be the mechanism underlying these diverse processes is that neurogenesis occurs on a similar time scale to the representational drift in PCx, and the turnovers of abGCs is highly experience dependent [9] which is also reflected in the PCx drift [24]. More frequent exposure to the same odor

slows down the representational drift in PCx, while the drift rate increases again once this frequent exposure was halted [24].

We therefore hypothesized that the long-term plasticity conferred by adult-neurogenesis in MOB percolates through the olfactory system serving as the mechanism of representational drift in PCx. To test this hypothesis, we used a spiking neuronal network model that replicated the circuit architecture within and between the MOB and PCx, integrating both the ongoing network restructuring due to adult-neurogenesis and the short-term plasticity of abGCs. We found that adult-neurogenesis differentially modulated odor responses and representations in M/T cells in the MOB and PCs in PCx. While the MOB maintained stable population representations despite changes in individual M/T cell responses due to neurogenesis, the PCx shows variation at both individual and population levels, leading to representational drift. Furthermore, when we incorporated spike-timing-dependent plasticity (STDP) at the synapses on abGCs, repeated odor exposure stabilized the PCx representations resulting in a reduction in drift rate. Taken together, we identified how the rules of plasticity on short-term time scales such as STDP and long-term time scales like adult-neurogenesis allow networks to both preserve sensory representations in some circuits like the MOB, while allowing other representations to change like those in PCx. Our work reveals the nuanced role played by adult-neurogenesis in balancing stability and adaptability in the chemosensory system.

Results

Spiking network model of adult-neurogenesis in early olfactory system

To understand the functional role of adult-neurogenesis of GCs on the odor representations in both MOB and PCx, we used a detailed spiking neural model that recapitulates the circuit architecture and neural dynamics of the early olfactory system (**Fig.1A1**, Methods). To this, we added adult-neurogenesis, which we modeled as a process where a subset of granule cells are killed off and new granule cells are integrated into the network as abGCs (**Fig.1A1**) [7,28]. To do this, following elimination of 10% of the GCs in the network, we added new cells and randomly assigned synaptic weights between these abGCs and M/Ts, abGCs and other GCs or short axon cells (SACs), and the top-down feedback projections from PCs to abGCs (**Fig.1A2**). These new synaptic weights for abGCs were sampled from the same distributions that generated the initial network model, such that although individual weight values and connectivity were being modulated, the total distribution of synaptic weights remain stable (**Fig.1B2**). We simulated a total of 11 days of neurogenesis from Day-0 and Day-10 by which point almost all GCs in the model have gone through adult-neurogenesis. Over the course, the synaptic weights between M/Ts and GCs, GCs/SACs and GCs, PCs and GCs were changed to match the observed changes in experiments (**Fig.1B1-1B3, FigS1**). Although the empirical rate of adult-neurogenesis has been found to vary in rodent depending on the measurement approach and the behavioral paradigms being used [29], we selected a rate of 10% for a reasonable computational time. Notably, changing this rate in our model only affected the scale of the observations without qualitatively changing the core results. These gradual changes in the network connectivity allowed us to probe the long-term effect of adult-neurogenesis on odor processing and the effect it had on modulating odor representations in MOB and PCx over time.

Odors drive coordinated activity in structures called glomeruli from which M/T cells receive their information about the odors. To match the glomerular activation patterns both in terms of the identify and onset timing in response to real odors [30–32], we generated a panel of 100 model odors where each one activated 6%~20% of the total 50 glomeruli in the model with different onset latencies (**Fig.1C1, FigS1**). Each model odor was presented during a 250ms time window (4Hz sniff), corresponding to a single sniff that is ethologically and behaviorally relevant time-scale for rodents [33–35]. Our generated panel of model odors spanned a wide range of similarity, ranging from distinct odor pairs with low pairwise correlations (see Methods) to highly similar odor pairs with high pairwise correlations (**Fig.1C2**). The input to our network, the model odors at the glomerular level, remained unchanged across simulated days consistent with previous observations of stable odor responses of glomeruli [36]. Using this experimental paradigm, we could study how the same odor inputs were differently encoded for over the course of adult-neurogenesis by both the principal cells in the main olfactory bulb and the piriform cortex [14,37].

Modulation of individual cell responses and preservation of population representations in MOB

First, we examined how adult-neurogenesis affected the responses of both individual M/T cells in the bulb and the population. We found that individual M/T cells changed their responses to the same odor across days due to adult-neurogenesis, with some cells decreasing the firing rate responses (**Fig.2A1** top) while other cells increased the magnitude of their responses (**Fig.2A2** bottom, **Fig.S2**), similar to what has been observed by others using calcium imaging of M/T cell activity [36,38]. These changes in gain are consistent with a model of normalization, wherein the firing of an individual neurons is modulated within a regime. However, when we examined the M/T responses to the same odor across the population (**Fig.2B2**), we found that the overall pattern of population responses was preserved across days despite the ongoing neurogenesis. In this example, the odor activated 6 of the 50 glomeruli. Although individual M/T responses changed (**Fig.2A1, 2A2** arrows), the groups of M/T cells driven by the same glomerulus preserved the temporal structure of their firing as a whole. Each individual M/T cell received certain amount of inhibition from a subset of GCs. With the incorporation of abGCs that eliminates some connections, and randomly establishes new ones, the synaptic weights of abGCs changed the inhibition at the individual M/T cell level, but preserved the distribution of inhibition across the population of M/T cells associated with a each glomerulus. As a result, adult neurogenesis effectively preserved the ensemble response to each odor for M/T cells associated with a single glomerulus, but led to a reshuffling of the identity of which M/T cells responded at what time epoch and with what magnitude.

Next, we wanted to quantify the changes in M/T odor response across days due to adult-neurogenesis. We took the odor-evoked firing rate over the 250ms time window across all M/T cells an ensemble vector, and computed their correlation between Day-0 and each other day. We named this correlation as "*full-ensemble correlation*". Regardless of using either single-trial (**Fig.2A3**) or trial-averaged responses (**Fig.2A4**), the within-odor full-ensemble correlation decreased significantly over time. This decrease is consistent with experimental observations [38]. The across-odor correlations, computed

175 from responses evoked by different odors, remained low across all days (**Fig.2A4**).
176 Therefore, these results indicated that the gradual changes in the odor-evoked responses
177 of individual M/T cells (**Fig.2A1**) accumulated over time.
178 However, as we observed above, the overall pattern of M/T population responses
179 was preserved (**Fig.2A2**), suggesting that the covariance, a measure of the shared
180 fluctuations across M/T population might remain stable. To test this, we projected M/T
181 population responses into a low-dimensional space (**Fig.2B1, 2B2,** see Methods), where
182 the time varying odor-evoked responses across the population constituted a trajectory in
183 the odor representation space of M/T cell population activity. For the two example odors,
184 the M/T trajectories of the same odor stayed quite close on the two example days
185 (**Fig.2B1**). If we simplified the single-trial trajectories by only plotting the maximal-distance
186 points to the origin (**Fig.2B2**), we found that the points of the same odor (color) stayed
187 clustered together in the space across all days (darkness of the color) despite the ongoing
188 circuit restricting due to adult-neurogenesis. The correlation of the low-dimensional
189 trajectories, which we named as "*reduced-space correlation*", remained high across all
190 days (**Fig.2B3**), and only dropped to ~0.7-0.8 on Day-10 (**Fig.2B4**). This is consistent
191 with a number of recent experimental studies using calcium-imaging on M/T cells [38,39].
192 Together, our results showed that although adult-neurogenesis gradually varied the
193 responses of individual M/T cells, the low-dimensional representations of M/T cells in the
194 reduced space remained were stable across days despite the changes in local synaptic
195 organization due to adult-neurogenesis.
196
197 **Modulation of both individual cell responses and population representations in**
198 **PCx**
199 M/T cells in MOB send random projections to PCx, such that each individual piriform cell
200 receives input from a random subset of M/T cells associated with different glomeruli [4,6].
201 PCx cells incorporate this feedforward information about odor identity and concentration
202 from the individual M/T cells in the MOB [14] and assembles those components into an
203 olfactory percept [21,23]. Although perceptual stability is a hallmark of sensory processing
204 and piriform cortex has historically been thought to be a place where perceptual stability
205 is established in the population code, recent evidence has started to challenge this idea
206 [24]. We hypothesized that the gradual changes in the individual M/T responses, passed
207 through the nonlinearities of synaptic integration, would affect the responses of PCs at
208 both individual and population level. We studied this by looking at the activity of individual
209 PCs and the ensembles of PCs in PCx.
210 Similar to M/T cells, the responses of individual PCs to the same odor varied
211 across days. Some PCs increased their responses while others decreased responses
212 (**Fig.3A1**, **Fig.S3**), consistent with recent chronic recordings in PCx (**Fig.S4**) [24]. However,
213 unlike M/T cells, the overall pattern of PCs responses varied as a result of adult-
214 neurogenesis (**Fig.3A2**). Some PCs responding strongly on Day-1 became inactive on
215 Day-9, whereas some PCs not responding on Day-1 became strongly activated on Day-
216 9. Consequently, the combinatorial patterns of activated PCs by the same odor were
217 reorganized by adult-neurogenesis on different days. Additionally, we also found that the
218 temporal structure of firing rate in individual PCs was highly variable. For example, some
219 PCs changed the onset and duration of their activation over the course of neurogenesis
220 (**Fig.3A2**). As a consequence, the within-odor full-ensemble correlation showed a

221 significant drop for PCs (**Fig.3A3, 3A4**). This is consistent with recent studies examining
222 the responses of PCs over time and demonstrating that patterns of PCs responses in
223 both individual cells and populations of cells can *drift* over time [24].
224 Changes in the firing rates reflect the changes in the variance of individual cells
225 (**Fig.S5**), but they do not say anything about the covariance, nor do they capture the
226 nonlinear interactions that shape the representations in PC populations when synaptic
227 information is integrated across M/T cell inputs and passes through the threshold
228 nonlinearity in individual PCs reflective of this integration. To study this, we calculated
229 the covariance across population of PCs was impacted by adult-neurogenesis. In
230 contrast to the M/T population where the representational trajectories of the same odor
231 followed one another closely in the space across different days, we found that the low-
232 dimensional trajectories of PCs showed a large variability across different days (**Fig.3B1**).
233 As a result, the maximal-distance for the trajectories on each day were broadly spread in
234 the space across progressive days of neurogenesis (**Fig.3B2**). These results are
235 consistent with representational drift in the odor encoding space. Quantitatively, the
236 within-odor reduced-space correlation decreased substantially across days (**Fig.3B3,**
237 **3B4**). Our data suggests that as a consequence of both the random projections of M/T
238 cells to different PCs and the ways in which the cortical cells integrate those inputs, PCx
239 representations drift with ongoing adult neurogenesis in the bulb.
240 Next, we asked how adult-neurogenesis geometrically reshaped the odor manifold
241 and representational trajectories in the high-dimensional space? Recent computational
242 models that have been built on longstanding frameworks of population coding suggest
243 that neural representations reside in a high-dimensional manifold [40,41]. First, we reasoned
244 that the structure of the odor manifold would be defined as the aggregation of the odor-
245 evoked temporal responses within a sniff cycle to all the odors based on evidence
246 showing that different odors evoke complex and distinct temporal activities in both M/T
247 cells [42–44] and PCs [45–47]. For visualization, we plotted the odor manifold in the three-
248 dimensional PCA space (**Fig.S6**). We found the odor manifolds of M/T cells were highly
249 overlapping with each other, whereas for PCs they were much more separated. Across
250 individual odors, we quantified the geometrical reshaping of representational trajectories
251 by calculating the cosine similarity (see **Methods**) which measures the similarity between
252 two vectors. It has a value 1 if the two vectors have the same direction, and a value 0 if
253 they are orthogonal. We found that cosine similarity using the population firing rate of
254 M/T cells and PCs had a similar degree of decrease as the function of intervals (i.e.,
255 number of days between two representations) (**Fig.S7A1**). However, the cosine similarity
256 using representational trajectories remained stable for M/T cell but reduced for PCs
257 (**Fig.S7B1**).
258 If representations drift as a result of adult-neurogenesis, then behaviors too should
259 be impacted, drifting in a similar time-scale. To unpack this connection, we used the K-
260 nearest neighbor algorithm as the decoder (see **Methods**). We found that the decoding
261 accuracy for discriminating two different odors using M/T cell population responses was
262 high but accuracy in PCs dropped substantially capturing the representational flexibility
263 in PCx (**Fig.S7**).
264
265 **Experience-dependent plasticity enhances representational stability in PCx**

So far, we have shown that adult-neurogenesis, a process that changes the circuit structure of the early olfactory system, is one mechanism by which representational drift in PCx happens. Interestingly, it has been reported that repeated experience of an odorant stabilizes odor representations and thus reduces the drift in PCx [24]. The mechanism which drives drift also appears to stabilize that drift when the olfactory environment is stable, suggesting that a core feature of the mechanism should be plasticity. Since the synapses of abGCs have been shown to be highly plastic and experience-dependent [8,9,48], we reasoned that experience-dependent plasticity of the same abGCs that drive representational in PCx may also stabilize that drift in response to the experience of encountering a stable olfactory environment.

To model experience-dependent changes at the level of synapses, we implemented a spike-timing-dependent plasticity (STDP) rule [49–51] across the diversity of the synapses related to an abGC (**Fig.4A1**). Depending on the spike timing interval of pre- and post-synaptic neurons, the synaptic weight could be either facilitated or suppressed (**Fig.4A2**, see Methods). Experience then was modeled as repeated presentations of the same set of odors every day (50 trials for each odor per day) to our network model, while adult-neurogenesis was occurring as previously described, with the network presumably learning these stable representations in the pattern of synaptic connectivity. In this example GC, the adult-neurogenesis that took place on day-4, resulted in a new cell being added to the circuit, while the existing cell was removed, a process that randomly reset a group of synaptic weights (say, S1 and S2, **Fig.4B**) across two days of neurogenesis. Without STDP, the synaptic weights S1 and S2 would keep constant or fluctuate by some stochastic process, regardless of what was happening in the environment, including the effects of the repeated experience of an odor (black line, **Fig.4B**). The implementation of STDP meant that the synaptic weight may change on a trial-by-trial basis when an odor was repeatedly presented (blue line, **Fig.4B**). In the end, the weight S1 may be enhanced while the weight S2 may be suppressed. Although odor representations of M/T cells remained stable with and without STDP (**Fig.4C1**), we found that odor representations in PCx was stabilized with STDP (**Fig.4C2**). The correlation drops from day-0 was significantly reduced (0.8 without STDP and 0.4 with STDP by day-10, **Fig.4C2** left), and the drift rate (° per day), which quantified the daily angle changes of the population responses (see **Methods**), was reduced by 26% (7.9 without STDP and 5.8 without STDP, **Fig.4C2** right). Adding STDP to the network and using repeated presentations of an odor meant that the synapses that would otherwise randomly change due to adult-neurogenesis converged asymptotically to some weight (**Fig.S8**). Importantly, we identified that while the brain is constantly undergoing change, especially in the MOB and the PCx due to ongoing adult-neurogenesis, the impact of these changes on both population responses and the representation depends as much on the plasticity rules as it does on the ongoing statistics of the environment.

Discussion

In our study, we modeled adult-neurogenesis as a dynamic reshuffling of granule cells (GCs) within a detailed spiking neuronal network that replicated the circuit architecture of the main olfactory bulb (MOB) and piriform cortex (PCx). This modeling revealed how

adult-neurogenesis differentially modulates odor responses and representations in mitral and tufted (M/T) cells and PCs.

In the MOB, individual M/T cells exhibited variable odor responses akin to gain control, altering their firing rate magnitudes over time. This is consistent with earlier experimental studies using calcium-imaging [36,38,39]. Despite these fluctuations, the overall pattern of M/T cells population responses remained stable. This stability is attributed to consistent glomerular input, as reflected in the low-dimensional M/T cell trajectories and their proximity in reduced PCA space. This stability of M/T cells we observed in the reduced space is consistent with a recent experimental study [39] using both linear (PCA) and nonlinear (t-SNE) dimensionality reduction methods. Conversely, in the PCx, both individual and population patterns of PCs responses were in constant flux due to the ongoing adult-neurogenesis. This resulted in a geometric reshaping of odor representations and a drift in the odor manifold defined by those representations, consistent with experimental finding[24]. Our results reveal how the process of adult-neurogenesis may support a number of computations in the early olfactory circuits, including how a sensory representation may remain stable, and how it might change due to plasticity.

Second, we found that one for of the roles for STDP in the early olfactory system is reducing representational drift in the PCx. Repeated exposure to an odor significantly reduced the representational drift in the PCx, consistent with experimental observations [24]. Rather counterintuitively, this result suggests that a role of STDP and plasticity in general is stabilizing representations despite ongoing changes in the circuit. Here, representational stability arises because of the stability of the sensory world; Representational permanence, rather than being a feature of the circuit, is a feature of the sensory landscape, a stabilizing force against the inherent variability introduced by continuous adult neurogenesis. Adult-neurogenesis, which occurs throughout the animal's life, may confer a mechanistically different computational framework as compared to vision or audition, for which critical periods delineate the bounds of plasticity, and define the periods over which sensory representations are changed or stabilized.

In addition to PCx, M/T cells also project to other cortical areas such as the anterior olfactory nucleus (AON). Although in our model we didn't differentiate mitral and tufted cells as did in many early experiment, it has been recently reported that mitral and tufted cells have distinct preferred cortical targets, with mitral cells targeting more at PCx and tufted cells targeting more at AON [52]. The authors also found that tufted cells substantially outperform mitral cells in decoding both odor identity and intensity, suggesting that tufted cells and their targeted AON are more ideal to compute odor identity than the mitral cells and PCx [52]. One possible reason for such differences might be: mitral cells are located in the deeper layers of the bulb and thus they interact primarily with abGCs, whereas tufted cells in the superficial layer preferentially interact with existing GCs that were born in the neonatal period [53,54]. Therefore, the activity of mitral cells may be more impacted by the turn-overs of abGCs, and the effect of adult-neurogenesis then percolates onto PCx. Comparatively, adult-neurogenesis has less impact on the tufted cells targeting more at the AON, potentially contributing to the better performance in encoding odors in AON.

While our study focused on the effects of adult-neurogenesis in the olfactory bulb on odor representations, it does not negate the possibility of other forms of plasticity [55]

contributing to the representational drift observed in the PCx [24]. Indeed, similar representational drifts have been noted in other brain areas like the posterior parietal cortex (PPC) [56], primary motor cortex [57], and hippocampus [58,59]. Of these regions, adult-neurogenesis only occurs in the hippocampus, where adult-born granule cells integrate into the existing circuitry of dentate gyrus [60]. Interestingly, similar to what we our model demonstrated for the early olfactory system (i.e., new-born cells in MOB and drift in PCx), the cells downstream of the dentate in the CA3 region [61] and CA1 region [27,58,59] have been found to drift over days and weeks.

Both PCx and hippocampus are evolutionarily old archicortical structures. This conservation of adult-neurogenesis in these brain regions may suggest a broader evolutionary strategy. This feature underscores the structural flexibility of these regions, which likely conferred selective advantages in navigating dynamic environments. The PCx specializes in processing olfactory information, enabling organisms to detect and discriminate between volatile chemical stimuli, while the hippocampus is crucial for spatial navigation and memory formation. By maintaining flexible neural structures, such as through adult-neurogenesis, these regions can rapidly update the representations of odors and spatial information, respectively, in response to changing environmental cues. This flexibility may enable the early organisms to effectively represent and adapt to the dynamic worlds they inhabited, enhancing their chances of survival and reproduction across evolutionary time scales [62–64]. However, as organisms evolved, brain regions such as the PPC, lacking significant adult-neurogenesis, might rely on alternative mechanisms to balance plasticity and stability [55].

In conclusion, our study not only elucidates a potential mechanism for representational drift in the PCx but also highlights the nuanced role of adult neurogenesis in maintaining the balance between stability and flexibility in olfactory system. The incorporation of STDP in abGCs, as evidenced by our model, emerges as a critical factor in modulating this balance, offering a new perspective on how the brain adapts to an ever-changing sensory environment.

Acknowledgments

This study was supported by funding from the National Institutes of Health (NIH) and the National Science Foundation (NSF). KP was funded by NIH R01 DC021141 and NSF CAREER 1749772. This manuscript has been released as a pre-print.

Author contributions

K.P. conceived and supervised the project. Z.C. performed the experiments and analyses. Z.C. and K.P. created the figures and wrote the manuscript. Both authors approved the submitted version.

Competing interests

The authors declare no competing interests.

397 ## References

398 1. Lledo, P.-M., Alonso, M. & Grubb, M. S. Adult neurogenesis and functional plasticity in neuronal
399 circuits. *Nat Rev Neurosci* **7**, 179–193 (2006).
400 2. Urban, N. N. & Sakmann, B. Reciprocal intraglomerular excitation and intra- and interglomerular
401 lateral inhibition between mouse olfactory bulb mitral cells. *The Journal of Physiology* **542**, 355–367
402 (2002).
403 3. Schoppa, N. E. & Urban, N. N. Dendritic processing within olfactory bulb circuits. *Trends in*
404 *Neurosciences* **26**, 501–506 (2003).
405 4. Sosulski, D. L., Bloom, M. L., Cutforth, T., Axel, R. & Datta, S. R. Distinct representations of olfactory
406 information in different cortical centres. *Nature* **472**, 213–216 (2011).
407 5. Ghosh, S. *et al.* Sensory maps in the olfactory cortex defined by long-range viral tracing of single
408 neurons. *Nature* **472**, 217–220 (2011).
409 6. Miyamichi, K. *et al.* Cortical representations of olfactory input by trans-synaptic tracing. *Nature* **472**,
410 191–196 (2011).
411 7. Lepousez, G., Valley, M. T. & Lledo, P.-M. The Impact of Adult Neurogenesis on Olfactory Bulb
412 Circuits and Computations. *Annu. Rev. Physiol.* **75**, 339–363 (2013).
413 8. Lepousez, G. *et al.* Olfactory learning promotes input-specific synaptic plasticity in adult-born
414 neurons. *Proceedings of the National Academy of Sciences* **111**, 13984–13989 (2014).
415 9. Livneh, Y. & Mizrahi, A. Experience-dependent plasticity of mature adult-born neurons. *Nat Neurosci*
416 **15**, 26–28 (2012).
417 10. Nissant, A., Bardy, C., Katagiri, H., Murray, K. & Lledo, P.-M. Adult neurogenesis promotes synaptic
418 plasticity in the olfactory bulb. *Nat Neurosci* **12**, 728–730 (2009).
419 11. Lledo, P.-M. & Valley, M. Adult Olfactory Bulb Neurogenesis. *Cold Spring Harb Perspect Biol* **8**,
420 a018945 (2016).

421 12. Breton-Provencher, V., Lemasson, M., Peralta, M. R. & Saghatelyan, A. Interneurons produced in
422 adulthood are required for the normal functioning of the olfactory bulb network and for the
423 execution of selected olfactory behaviors. *Journal of Neuroscience* **29**, 15245–15257 (2009).
424 13. Kouremenou, I., Piper, M. & Zalucki, O. Adult Neurogenesis in the Olfactory System: Improving
425 Performance for Difficult Discrimination Tasks? *BioEssays* **42**, 2000065 (2020).
426 14. Bekkers, J. M. & Suzuki, N. Neurons and circuits for odor processing in the piriform cortex. *Trends in*
427 *Neurosciences* **36**, 429–438 (2013).
428 15. Choi, G. B. *et al.* Driving Opposing Behaviors with Ensembles of Piriform Neurons. *Cell* **146**, 1004–
429 1015 (2011).
430 16. Smear, M., Resulaj, A., Zhang, J., Bozza, T. & Rinberg, D. Multiple perceptible signals from a single
431 olfactory glomerulus. *Nat Neurosci* **16**, 1687–1691 (2013).
432 17. Chong, E. *et al.* Manipulating synthetic optogenetic odors reveals the coding logic of olfactory
433 perception. *Science* **368**, eaba2357 (2020).
434 18. Gill, J. V. *et al.* Precise Holographic Manipulation of Olfactory Circuits Reveals Coding Features
435 Determining Perceptual Detection. *Neuron* **108**, 382-393.e5 (2020).
436 19. Mombaerts, P. *et al.* Visualizing an Olfactory Sensory Map. *Cell* **87**, 675–686 (1996).
437 20. Buck, L. & Axel, R. A novel multigene family may encode odorant receptors: a molecular basis for
438 odor recognition. *Cell* **65**, 175–187 (1991).
439 21. Davison, I. G. & Ehlers, M. D. Neural Circuit Mechanisms for Pattern Detection and Feature
440 Combination in Olfactory Cortex. *Neuron* **70**, 82–94 (2011).
441 22. Stern, M., Bolding, K. A., Abbott, L. & Franks, K. M. A transformation from temporal to ensemble
442 coding in a model of piriform cortex. *eLife* **7**, e34831 (2018).
443 23. Pashkovski, S. L. *et al.* Structure and flexibility in cortical representations of odour space. *Nature*
444 **583**, 253–258 (2020).

445 24. Schoonover, C. E., Ohashi, S. N., Axel, R. & Fink, A. J. P. Representational drift in primary olfactory
446 cortex. *Nature* **594**, 541–546 (2021).
447 25. Kanter, E. D. & Haberly, L. B. NMDA-dependent induction of long-term potentiation in afferent and
448 association fiber systems of piriform cortex in vitro. *Brain research* **525**, 175–179 (1990).
449 26. Jung, M. W. & Larson, J. Further characteristics of long-term potentiation in piriform cortex. *Synapse*
450 **18**, 298–306 (1994).
451 27. Ziv, Y. *et al.* Long-term dynamics of CA1 hippocampal place codes. *Nature neuroscience* **16**, 264–266
452 (2013).
453 28. Aimone, J. B. & Gage, F. H. Modeling new neuron function: a history of using computational
454 neuroscience to study adult neurogenesis. *European Journal of Neuroscience* **33**, 1160–1169 (2011).
455 29. Pignatelli, A. & Belluzzi, O. Neurogenesis in the Adult Olfactory Bulb. in *The Neurobiology of*
456 *Olfaction* (ed. Menini, A.) (CRC Press/Taylor & Francis, Boca Raton (FL), 2010).
457 30. Fantana, A. L., Soucy, E. R. & Meister, M. Rat Olfactory Bulb Mitral Cells Receive Sparse Glomerular
458 Inputs. *Neuron* **59**, 802–814 (2008).
459 31. Gschwend, O., Beroud, J., Vincis, R., Rodriguez, I. & Carleton, A. Dense encoding of natural odorants
460 by ensembles of sparsely activated neurons in the olfactory bulb. *Sci Rep* **6**, 36514 (2016).
461 32. Vincis, R., Gschwend, O., Bhaukaurally, K., Beroud, J. & Carleton, A. Dense representation of natural
462 odorants in the mouse olfactory bulb. *Nat Neurosci* **15**, 537–539 (2012).
463 33. Rinberg, D., Koulakov, A. & Gelperin, A. Speed-Accuracy Tradeoff in Olfaction. *Neuron* **51**, 351–358
464 (2006).
465 34. Uchida, N. & Mainen, Z. F. Speed and accuracy of olfactory discrimination in the rat. *Nat Neurosci* **6**,
466 1224–1229 (2003).
467 35. Wesson, D. W., Carey, R. M., Verhagen, J. V. & Wachowiak, M. Rapid Encoding and Perception of
468 Novel Odors in the Rat. *PLoS Biol* **6**, e82 (2008).

469 36. Kato, H. K., Chu, M. W., Isaacson, J. S. & Komiyama, T. Dynamic Sensory Representations in the
470 Olfactory Bulb: Modulation by Wakefulness and Experience. *Neuron* **76**, 962–975 (2012).
471 37. Uchida, N., Poo, C. & Haddad, R. Coding and Transformations in the Olfactory System. *Annu. Rev.*
472 *Neurosci.* **37**, 363–385 (2014).
473 38. Yamada, Y. *et al.* Context- and Output Layer-Dependent Long-Term Ensemble Plasticity in a Sensory
474 Circuit. *Neuron* **93**, 1198-1212.e5 (2017).
475 39. Shani-Narkiss, H., Beniaguev, D., Segev, I. & Mizrahi, A. Stability and flexibility of odor
476 representations in the mouse olfactory bulb. *Front. Neural Circuits* **17**, (2023).
477 40. Langdon, C., Genkin, M. & Engel, T. A. A unifying perspective on neural manifolds and circuits for
478 cognition. *Nat Rev Neurosci* 1–15 (2023) doi:10.1038/s41583-023-00693-x.
479 41. Kriegeskorte, N. & Wei, X.-X. Neural tuning and representational geometry. *Nat Rev Neurosci* **22**,
480 703–718 (2021).
481 42. Baker, K. L., Vasan, G., Gumaste, A., Pieribone, V. A. & Verhagen, J. V. Spatiotemporal dynamics of
482 odor responses in the lateral and dorsal olfactory bulb. *PLoS Biol* **17**, e3000409 (2019).
483 43. Gire, D. H. *et al.* Temporal Processing in the Olfactory System: Can We See a Smell? *Neuron* **78**, 416–
484 432 (2013).
485 44. Schaefer, A. T. & Margrie, T. W. Spatiotemporal representations in the olfactory system. *Trends in*
486 *Neurosciences* **30**, 92–100 (2007).
487 45. Rennaker, R. L., Chen, C.-F. F., Ruyle, A. M., Sloan, A. M. & Wilson, D. A. Spatial and Temporal
488 Distribution of Odorant-Evoked Activity in the Piriform Cortex. *Journal of Neuroscience* **27**, 1534–
489 1542 (2007).
490 46. Chen, Z. & Padmanabhan, K. Top-down feedback enables flexible coding strategies in the olfactory
491 cortex. *Cell Reports* **38**, 110545 (2022).

47. Haddad, R. *et al.* Olfactory cortical neurons read out a relative time code in the olfactory bulb. *Nat Neurosci* **16**, 949–957 (2013).

48. Wu, A. *et al.* Context-dependent plasticity of adult-born neurons regulated by cortical feedback. *Sci. Adv.* **6**, eabc8319 (2020).

49. Froemke, R. C. & Dan, Y. Spike-timing-dependent synaptic modification induced by natural spike trains. *Nature* **416**, 433–438 (2002).

50. Bi, G. & Poo, M. Synaptic Modification by Correlated Activity: Hebb's Postulate Revisited. *Annual Review of Neuroscience* **24**, 139–166 (2001).

51. Markram, H., Gerstner, W. & Sjöström, P. J. Spike-Timing-Dependent Plasticity: A Comprehensive Overview. *Front. Synaptic Neurosci.* **4**, (2012).

52. Chae, H., Banerjee, A., Dussauze, M. & Albeanu, D. F. Long-range functional loops in the mouse olfactory system and their roles in computing odor identity. *Neuron* S0896627322008108 (2022) doi:10.1016/j.neuron.2022.09.005.

53. Lemasson, M., Saghatelyan, A., Olivo-Marin, J.-C. & Lledo, P.-M. Neonatal and adult neurogenesis provide two distinct populations of newborn neurons to the mouse olfactory bulb. *Journal of Neuroscience* **25**, 6816–6825 (2005).

54. Whitman, M. C. & Greer, C. A. Adult neurogenesis and the olfactory system. *Progress in Neurobiology* **89**, 162–175 (2009).

55. Qin, S. *et al.* Coordinated drift of receptive fields in Hebbian/anti-Hebbian network models during noisy representation learning. *Nat Neurosci* **26**, 339–349 (2023).

56. Driscoll, L. N., Pettit, N. L., Minderer, M., Chettih, S. N. & Harvey, C. D. Dynamic reorganization of neuronal activity patterns in parietal cortex. *Cell* **170**, 986–999 (2017).

57. Rokni, U., Richardson, A. G., Bizzi, E. & Seung, H. S. Motor learning with unstable neural representations. *Neuron* **54**, 653–666 (2007).

516 58. Lee, J. S., Briguglio, J. J., Cohen, J. D., Romani, S. & Lee, A. K. The statistical structure of the
517 hippocampal code for space as a function of time, context, and value. *Cell* **183**, 620–635 (2020).
518 59. Gonzalez, W. G., Zhang, H., Harutyunyan, A. & Lois, C. Persistence of neuronal representations
519 through time and damage in the hippocampus. *Science* **365**, 821–825 (2019).
520 60. Toda, T., Parylak, S. L., Linker, S. B. & Gage, F. H. The role of adult hippocampal neurogenesis in
521 brain health and disease. *Mol Psychiatry* **24**, 67–87 (2019).
522 61. Hainmueller, T. & Bartos, M. Parallel emergence of stable and dynamic memory engrams in the
523 hippocampus. *Nature* **558**, 292–296 (2018).
524 62. Gonçalves, J. T., Schafer, S. T. & Gage, F. H. Adult Neurogenesis in the Hippocampus: From Stem
525 Cells to Behavior. *Cell* **167**, 897–914 (2016).
526 63. Jurkowski, M. P. *et al.* Beyond the Hippocampus and the SVZ: Adult Neurogenesis Throughout the
527 Brain. *Frontiers in Cellular Neuroscience* **14**, (2020).
528 64. Sailor, K. A., Schinder, A. F. & Lledo, P.-M. Adult neurogenesis beyond the niche: its potential for
529 driving brain plasticity. *Current Opinion in Neurobiology* **42**, 111–117 (2017).
530 65. Izhikevich, E. M. Simple model of spiking neurons. *IEEE Trans. Neural Netw.* **14**, 1569–1572 (2003).
531 66. Connors, B. W. & Gutnick, M. J. Intrinsic firing patterns of diverse neocortical neurons. *Trends in*
532 *Neurosciences* **13**, 99–104 (1990).
533 67. Padmanabhan, K. & Urban, N. N. Disrupting information coding via block of 4-AP-sensitive
534 potassium channels. *Journal of Neurophysiology* **112**, 1054–1066 (2014).
535 68. Burton, S. D. & Urban, N. N. Rapid Feedforward Inhibition and Asynchronous Excitation Regulate
536 Granule Cell Activity in the Mammalian Main Olfactory Bulb. *Journal of Neuroscience* **35**, 14103–
537 14122 (2015).

538 69. Egger, V., Svoboda, K. & Mainen, Z. F. Dendrodendritic Synaptic Signals in Olfactory Bulb Granule
539 Cells: Local Spine Boost and Global Low-Threshold Spike. *Journal of Neuroscience* **25**, 3521–3530
540 (2005).
541 70. Gibson, J. R., Beierlein, M. & Connors, B. W. Two networks of electrically coupled inhibitory neurons
542 in neocortex. *Nature* **402**, 75–79 (1999).
543 71. Suzuki, N. & Bekkers, J. M. Microcircuits Mediating Feedforward and Feedback Synaptic Inhibition in
544 the Piriform Cortex. *Journal of Neuroscience* **32**, 919–931 (2012).
545 72. Kapoor, V. & Urban, N. N. Glomerulus-Specific, Long-Latency Activity in the Olfactory Bulb Granule
546 Cell Network. *Journal of Neuroscience* **26**, 11709–11719 (2006).
547 73. Dhawale, A. K., Hagiwara, A., Bhalla, U. S., Murthy, V. N. & Albeanu, D. F. Non-redundant odor
548 coding by sister mitral cells revealed by light addressable glomeruli in the mouse. *Nat Neurosci* **13**,
549 1404–1412 (2010).
550 74. Koulakov, A. A. & Rinberg, D. Sparse Incomplete Representations: A Potential Role of Olfactory
551 Granule Cells. *Neuron* **72**, 124–136 (2011).
552 75. Lledo, P.-M., Gheusi, G. & Vincent, J.-D. Information Processing in the Mammalian Olfactory System.
553 *Physiological Reviews* **85**, 281–317 (2005).
554 76. Wachowiak, M., Denk, W. & Friedrich, R. W. Functional organization of sensory input to the
555 olfactory bulb glomerulus analyzed by two-photon calcium imaging. *PNAS* **101**, 9097–9102 (2004).
556 77. Padmanabhan, K. *et al.* Diverse Representations of Olfactory Information in Centrifugal Feedback
557 Projections. *Journal of Neuroscience* **36**, 7535–7545 (2016).
558 78. Sailor, K. A. *et al.* Persistent Structural Plasticity Optimizes Sensory Information Processing in the
559 Olfactory Bulb. *Neuron* **91**, 384–396 (2016).
560 79. Wanner, A. A. & Friedrich, R. W. Whitening of odor representations by the wiring diagram of the
561 olfactory bulb. *Nat Neurosci* **23**, 433–442 (2020).

562 80. Willhite, D. C. *et al.* Viral tracing identifies distributed columnar organization in the olfactory bulb.
563 *Proceedings of the National Academy of Sciences* **103**, 12592–12597 (2006).
564 81. Egger, V. & Urban, N. N. Dynamic connectivity in the mitral cell–granule cell microcircuit. *Seminars*
565 *in Cell & Developmental Biology* **17**, 424–432 (2006).
566 82. Schoppa, N. E. & Westbrook, G. L. AMPA autoreceptors drive correlated spiking in olfactory bulb
567 glomeruli. *Nat Neurosci* **5**, 1194–1202 (2002).
568 83. Soucy, E. R., Albeanu, D. F., Fantana, A. L., Murthy, V. N. & Meister, M. Precision and diversity in an
569 odor map on the olfactory bulb. *Nat Neurosci* **12**, 210–220 (2009).
570 84. Boyd, A. M., Sturgill, J. F., Poo, C. & Isaacson, J. S. Cortical Feedback Control of Olfactory Bulb
571 Circuits. *Neuron* **76**, 1161–1174 (2012).
572 85. Luna, V. M. & Schoppa, N. E. GABAergic Circuits Control Input-Spike Coupling in the Piriform Cortex.
573 *Journal of Neuroscience* **28**, 8851–8859 (2008).
574 86. Nunez-Parra, A., Maurer, R. K., Krahe, K., Smith, R. S. & Araneda, R. C. Disruption of centrifugal
575 inhibition to olfactory bulb granule cells impairs olfactory discrimination. *Proc Natl Acad Sci USA*
576 **110**, 14777–14782 (2013).
577 87. Otazu, G. H., Chae, H., Davis, M. B. & Albeanu, D. F. Cortical Feedback Decorrelates Olfactory Bulb
578 Output in Awake Mice. *Neuron* **86**, 1461–1477 (2015).
579 88. Padmanabhan, K. *et al.* Centrifugal Inputs to the Main Olfactory Bulb Revealed Through Whole Brain
580 Circuit-Mapping. *Front. Neuroanat.* **12**, 115 (2019).
581 89. Franks, K. M. *et al.* Recurrent Circuitry Dynamically Shapes the Activation of Piriform Cortex. *Neuron*
582 **72**, 49–56 (2011).
583 90. Large, A. M., Vogler, N. W., Mielo, S. & Oswald, A.-M. M. Balanced feedforward inhibition and
584 dominant recurrent inhibition in olfactory cortex. *Proc Natl Acad Sci USA* **113**, 2276–2281 (2016).

91. Padmanabhan, K. & Urban, N. N. Intrinsic biophysical diversity decorrelates neuronal firing while increasing information content. *Nat Neurosci* **13**, 1276–1282 (2010).

Figures and Tables

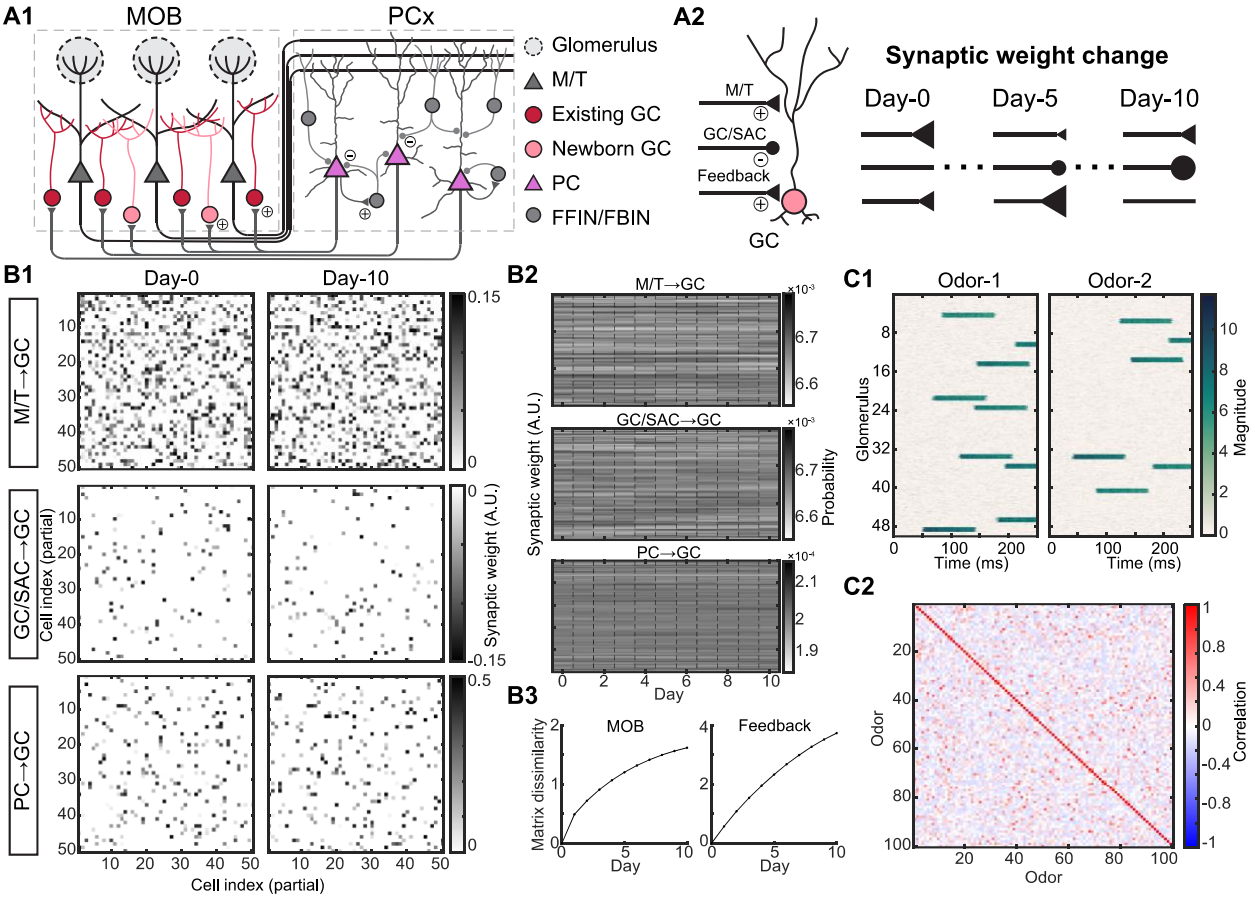

Figure 1. Spiking network model of adult-neurogenesis. (A1). Schematic of early olfactory circuit. M/T: mitral/tufted cells, GC: granule cells, abGCs: adult-born GCs, PCs: piriform cortical cell, FFIN: feedforward inhibitory neuron, FBIN: feedback inhibitory neuron. Example plus signs indicate excitatory synapses and minus signs indicate inhibitory synapses. (A2). Schematic of synaptic reshuffling of GCs due to adult-neurogenesis. On each day, 10% of GCs have their weights reshuffled, including the synaptic weights from M/T cells, other GCs or short-axon cells (SAC), and PCs to GC (feedback). (B1). Partial weight matrix on two example days between GCs and M/T cells (top), other GCs or SACs (middle), and feedback from PCs (bottom). (B2). Histograms of all synaptic weights across days. (B3). Weight matrix dissimilarity between Day-0 and each other day. (C1). An example model odor generated by stimulating different combinations of glomerular identity and timing of activation. (C2). Pair-wise correlations between model odors show the relative similarities and differences across all model odors.

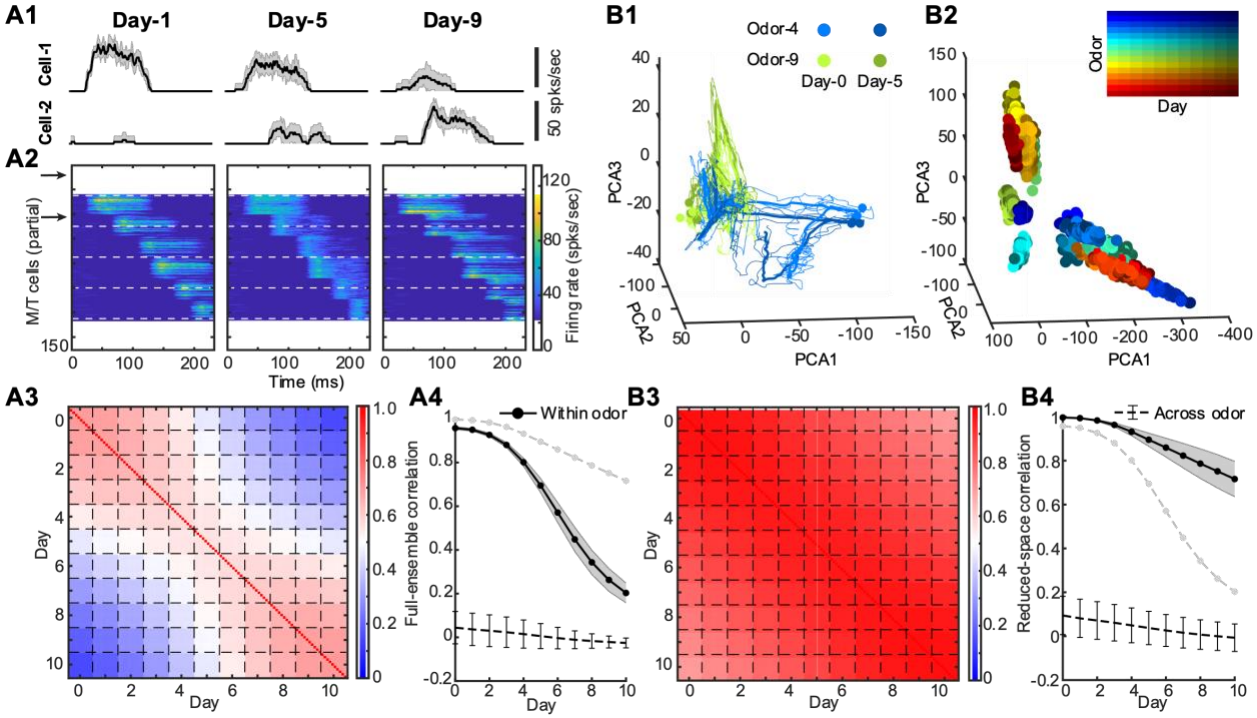

Figure 2. Adult-neurogenesis modulates individual M/T cell responses but preserves population representation. (A1). Trail-averaged firing rate of two example M/T cells responding to the same odor (within-odor) on three different days (mean ± SD, n = 10 trials). (A2). Firing rate patterns of odor-activated M/T cells to the same odor on three days. M/T cells driven by different glomeruli are separated by white dashed line. The two arrows correspond to the two example cells in (A1). (A3). Pairwise within-odor full-ensemble correlation of single-trial M/T cell responses between each day averaged across all odors (n = 100). Each small box separated by the dashed lines is a 10x10 matrix (n = 10 trials) corresponding to autocorrelation (same day on diagonal) and cross-correlation (different days off diagonal). (A4). Full-ensemble correlation of trial-averaged M/T cell responses for within-odor (black solid line with error bar: mean ± SD, n = 100 odors).) and across-odor (black dashed line with error bar: mean ± SD, n = 10 pairs) between Day-0 and each other day. Grey dashed line with no error bar: same as the black solid line in (B4). (B1). Low-dimensional trajectories of M/T responses to two example odors (color) on two different days (darkness of color). Thin curves: single-trial trajectories, thick curves: trial-averaged trajectories, points: maximal-distance points on trajectory to the origin. (B2). Only maximal-distance points are shown for different odors on different days. (B3). Similar to (A3) but for reduced-space correlation computed using the low-dimensional M/T trajectories (single-trial). (B4). Similar to (A4) but for reduced-space correlation computed using the low-dimensional M/T trajectories (trial-averaged). Grey dashed line with no error bar: same as the black solid line in (A4).

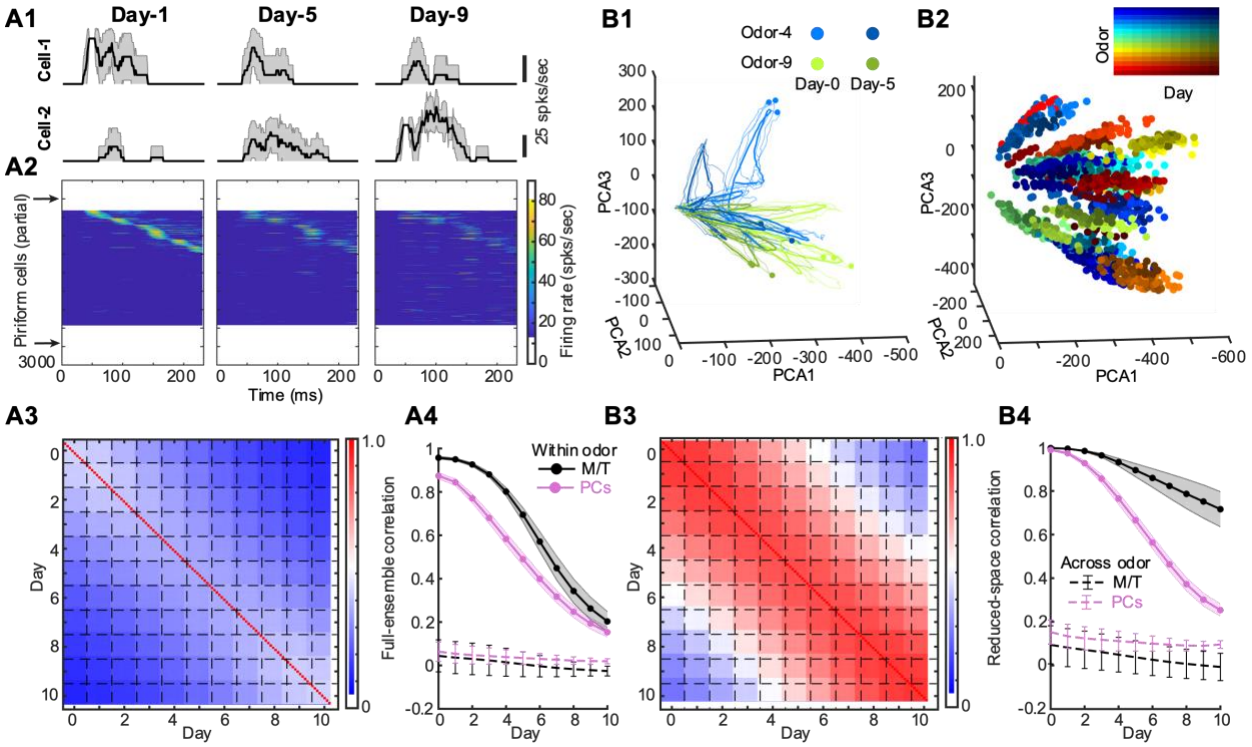

Figure 3. Adult-neurogenesis modulates both individual PCs responses and population representations. (A1). Trail-averaged firing rate of two example PCs responding to the same odor on three different days (mean ± SD, n = 10 trials). (A2). Firing rate patterns of partial PCs responding to the same odor on three days. The two arrows correspond to the two example cells in (A1). (A3). Pairwise within-odor full-ensemble correlation of single-trial PCs responses between each day averaged across all odors (n = 100). Each small box separated by the dashed lines is a 10x10 matrix (n = 10 trials) corresponding to autocorrelation (same day on diagonal) and cross-correlation (different days off diagonal). (A4). Full-ensemble correlation of trial-averaged cell (PCs: purple; M/T: black) responses for within-odor (solid line with error bar: mean ± SD, n = 100 odors).) and across-odor (dashed line with error bar: mean ± SD, n = 10 pairs) between Day-0 and each other day. The curves for M/T cells are the same lines as in Fig.2. (B1). Low-dimensional trajectories of PCs responses to two example odors (color) on two different days (darkness of color). Thin curves: single-trial trajectories, thick curves: trial-averaged trajectories, points: maximal-distance points on trajectory to the origin. (B2). Only maximal-distance points are shown for different odors on different days. (B3). Similar to (A3) but for reduced-space correlation computed using the single-trial PCA trajectories of PCs. (B4). Similar to (A4) but for reduced-space correlation computed using the trial-averaged PCA trajectories of PCs.

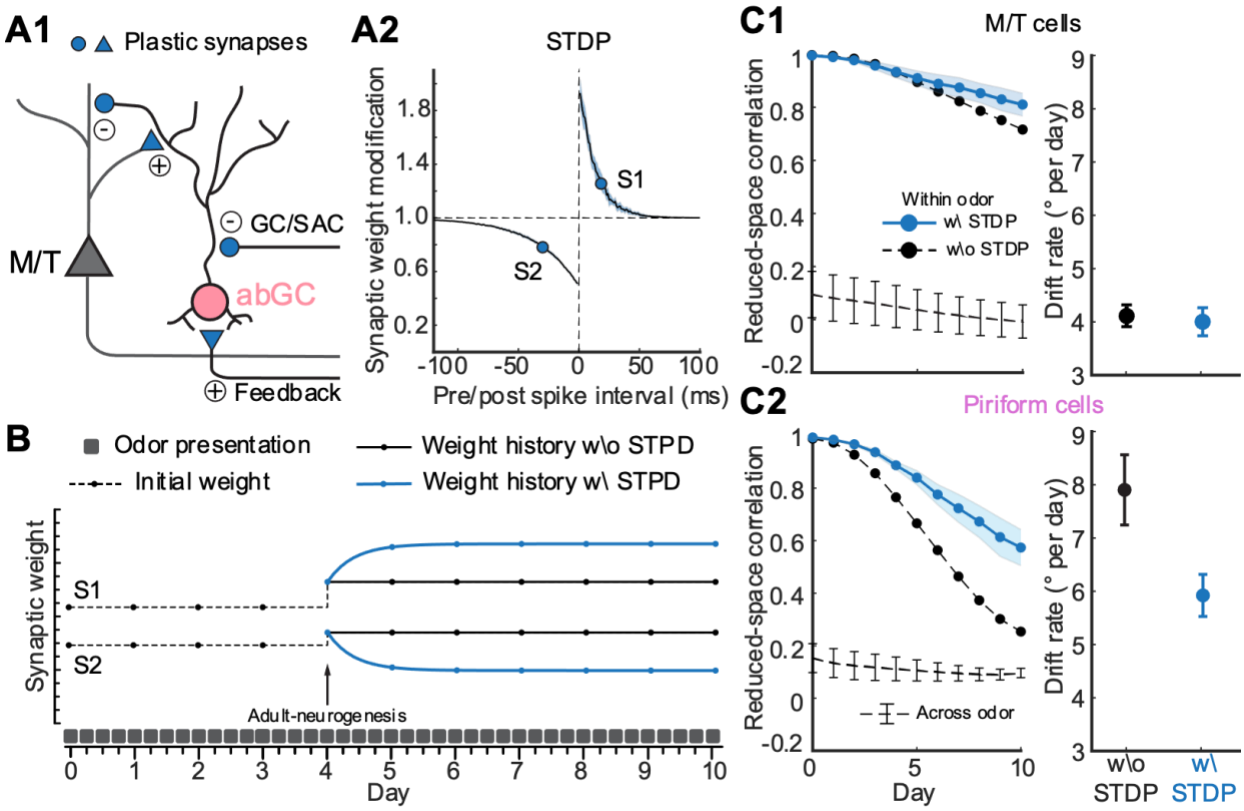

Figure 4. Experience-dependent plasticity enhances representational stability in PCx. (A1). Different types of plastic synapses (blue) related to an abGC. Circle: inhibitory; triangle: excitatory. (A2). Dependence of synaptic modification on pre/post inter-spike interval used for the spike-timing-dependent plasticity (STDP). S1 and S2 are two example synapses with different modification – S1: facilitated; S2: suppressed. (B). Weight history of the two example synapses in A2 when an odor is repeatedly presented. Adult-neurogenesis happens on day-4 which randomly resets the weights. The synaptic weights stay constant without plasticity (black) while change trial by trial with plasticity (blue). (C1). Left: reduced-space correlation of trial-averaged M/T trajectories between Day-0 and each day. Blue solid line with error bar: within-odor and with STDP (mean ± SD, n = 10 odors); black dashed line without error bar: within-odor and without STDP. Black dashed line with error bar: across-odors, mean ± SD, n = 10 pairs. Right: drift rate for M/T trajectories with and without STDP. (C2). Same as C1 but for PCs trajectories.

Methods

Organization and architecture of the model

The MOB consisted of 50 glomeruli (G) corresponding to the olfactory receptor neuron (ORN) inputs into the MOB [19]. Each glomerulus was connected to 25 mitral/tufted (M/T) cells for a total 1250 M/T cells. Within the MOB, a local population of 12,500 inhibitory granule cells (GCs) formed reciprocal and lateral inhibitory connections with M/T cells. Individual M/T cell "projections" formed random excitatory connections with 10,000 piriform cortical cells (PCs) in PCx. These PCs in turn "projected" back to the olfactory bulb, provided excitatory centrifugal feedback onto the inhibitory granule cells in the bulb. Within PCx, two types of inhibitory interneurons were included: a population of 1250 feedforward inhibitory neurons (FFIs) that received excitatory input from M/T cells and inhibited both PCs and other FFIs, and a population of 1250 local feedback inhibitory neurons (FBIs) that received input from a random subset of PCs and subsequently inhibited PCs and other FBIs.

Voltage dynamics of individual neurons

The voltage dynamics of individual cells in the network are modeled as spiking neurons [65] described by a two-dimensional (2D) system of ordinary differential equations of the form,

$$\frac{dv}{dt} = 0.04v^2 + 5v + 140 - u + I$$
$$\frac{du}{dt} = a(bv - u) \tag{1}$$

with the after-spiking resetting

$$\text{if } v \geq 30mV, \text{ then } v \leftarrow c, u \leftarrow u + d \tag{2}$$

Here v represents the voltage (mV) of the neuron and u represents a dimensionless membrane recovery variable accounting for the activation or inactivation of ionic currents; t is time and has unit of ms; a, b, c and d are the parameters by tuning which various firing patterns can be generated; I represents synaptic currents or injected dc-currents to the neuron.

We choose to use this neuron model to simulate the voltage dynamics of individual neurons because: 1). It combines the biological plausibility of the Hodgkin–Huxley neuron model and the computational efficiency of leaky integrate-and-fire neuron model, allowing us to simulate tens of thousands of spiking neurons simultaneously in our network; 2). Different combinations of the parameter values a, b, c and d can reproduce a diversity of firing patterns of neurons of known types, so we can capture the biophysical diversity in the firing properties for different types of neurons in olfactory system, such as the mitral/tufted (M/T) cells and granule cells in the main olfactory bulb (MOB), and piriform cortical cells and other local inhibitory interneurons in piriform cortex (PCx). In order to achieve heterogeneity such that different cells within the same type exhibit different dynamics, we introduced randomness in the parameter assignment (see Table 1). The r_i is a random variable uniformly distributed on the interval $[0,1]$ and i denotes the neuron index. For example, the parameter a will be distributed on the interval $[0.02, 0.1]$ within which various firing patterns can emerge. We also used r_i^2 or r_i^4 to bias the distribution to different extent for different cell types. Overall, based on our choice of parameters in the Izhikevich model, the spiking patterns of PCs and M/T cells largely fall into the category of regular spiking, intrinsically bursting or chattering neurons [21,66,67]. Inhibitory

neurons including GCs and FFIs/FBIs in the network can generate spiking patterns as fast spiking neurons and low-threshold spiking neurons [68–71].

Table 1 Parameters of Izhikevich neuron model for different cell types

	M/T cells	**GCs**	**PCs**	**FFIs/FBIs**
a	$0.1-0.08r_i^4$	$0.1-0.08r_i^2$	$0.02+0.08r_i$	$0.1-0.08r_i^2$
b	0.2	0.2	0.2	0.2
c	-65	$-65+15r_i^2$	-65	$-65+15r_i^2$
d	$2+6r_i^4$	2	$8-6r_i$	2

Synaptic input I to each neuron depends on the neuron type. For a cell i in MOB, I_i is a linear superposition of various sources

$$I_i = I_i^{mc-ex} + I_i^{gc-in} + I_i^{osn} + I_i^{feedback} + \xi_i \tag{3}$$

Here, I_i^{mc-ex} represents excitation from M/T cells and exists for both M/T cells and GCs. For GCs, when a M/T cells fires, the excitatory post-synaptic current (EPSC) I_i^{mc-ex} into different GCs are delayed by different latencies, resulting in different spiking latencies of GCs, consistent with previous experimental findings in the olfactory bulb granule cell network [72]. The I_i^{gc-in} represents inhibition from GCs and exists for both M/T cells and GCs. I_i^{osn} represents glomerular input and only exists for M/T cells. When a glomerulus is activated by a model odor, it provides correlated inputs I_i^{osn} to the M/T cells driven by that glomerulus. When a glomerulus is activated, the input current I_i^{osn} that an associated M/T cell receives is modelled as a step function with Gaussian noise added. Since each glomerulus receives inputs from a set of receptor neurons expressing the same olfactory gene type, the inputs to individual glomerulus from receptor neurons are substantially correlated [73–76]. Therefore, we assumed that the glomerular inputs to the apical dendrites received by the M/T cells associated with the same glomerulus were correlated. No input correlation between M/T cells associated with different glomeruli is assumed. $I_i^{feedback}$ represents excitatory centrifugal input from piriform cells and is non-zero only for GCs when feedback is ON. We set it to zero for all GCs when feedback is OFF. The ξ_i represents Gaussian white noise input with zero mean and standard deviation $\sigma = 1.75$ for M/T cells and $\sigma = 0.8$ for GCs.

Similarly, for a cell i in PCx, I_i is composed of

$$I_i = I_i^{mob} + I_i^{pc-ex} + I_i^{in} + \eta_i \tag{4}$$

where I_i^{mob} represents input from M/T cells in MOB and only exists for piriform cortical cells (PCs) and feedforward inhibitory neurons (FFIs); I_i^{pc-ex} represents excitation from PCs and exists for both PCs and feedback inhibitory neurons (FBIs); I_i^{in} represents inhibition from local inhibitory neurons including FFIs and FBIs; η_i represents Gaussian white noise input (zero mean and standard deviation $\sigma = 0.9$) and only exists for PCs.

Each action potential fired by a presynaptic neuron will evoke a jump in the corresponding synaptic inputs of all its postsynaptic targets by an amount equal to the appropriate synaptic strength. For example, action potentials of a M/T cell induce jumps in the excitatory currents of their postsynaptic target neurons, including I_i^{mc-ex} in M/T cells and GCs in MOB, and I_i^{mob} in FFIs and PCs in PCx. These synaptic inputs then decay to zero with time constant $10ms$. The height of the jump is determined by the pairwise

synaptic strength between any two neurons and their values are given in the synaptic weight matrix which will described in the next section.

Synaptic strength and model network architecture

The MOB consists of 50 glomeruli, each of which drives 25 M/T cells, thus a total 1250 M/T cells in MOB. Besides, a local population of 12,500 inhibitory GCs formed reciprocal and lateral inhibitory connections with M/T cells. Thus, within the MOB, we have a weight matrix $\mathbf{W}_{mob}$ of $13{,}750$ by $13{,}750$ with its entry W_{mob}^{ij} representing the synaptic strength from presynaptic neuron j to postsynaptic neuron i. Depending on the cell type, this matrix $\mathbf{W}_{mob}$ can be partitioned into four sub-matrices, i.e., from M/T cell to M/T cell, from M/T cell to GC, from GC to M/T cell and from GC to GC. The specific value of each entry in $\mathbf{W}_{mob}$ was assigned randomly according to two parameters we chose for each sub-matrix. One is the connection density (the percentage of non-zero synaptic weights) and the other is the average synaptic strength (mean of a uniform distribution from which individual synaptic weights are sampled). Each sub-matrix has its own value of the connection density and average synaptic strength. In particular, the connection density and average synaptic strength between M/T cells driven by the same glomerulus are higher than between M/T cells driven by different glomeruli.

Individual M/T cell "projections" form random excitatory connections with 10,000 PCs and 1250 FFIs in PCx, giving rise to a feedforward weight matrix $\mathbf{W}_{ff}$ of $11{,}250$ by 1250. Within PCx, PCs form recurrent excitations with each other. The FFIs inhibit both PCs and other FFIs, and another population of 1250 FBIs that receive input from a random subset of PCs inhibit PCs and other FBIs. Therefore, we have a matrix $\mathbf{W}_{pcx}$ of $12{,}500$ by $12{,}500$ that identifies all synaptic weights between cells in PCx. PCs "project" back to the MOB, providing excitatory centrifugal feedback to GCs, giving rise to a feedback weight matrix $\mathbf{W}_{fb}$ of $12{,}500$ by $10{,}000$. Under the condition of centrifugal feedback OFF, this $\mathbf{W}_{fb}$ is set to be a zero matrix. The connection density and average synaptic strength for all sub-matrices can be found in Table 2. The parameters are all chosen heuristically based on previous theoretical and experimental studies listed in Table 2.

Feedback projections from piriform cortex to the bulb may be structured, as retrograde rabies tracing demonstrates that piriform cells projecting to GC populations in the bulb tend to be spatially clustered [77]. Furthermore, a number of studies suggest that GC synapses are especially sensitive to plasticity [9,78], either through adult neurogenesis or more traditional mechanisms of synaptic reorganization. To implement all of these features, we structure the feedback projections to GCs such that the PCs receiving feedforward inputs from the M/T cells of certain glomeruli project back to the GCs which are reciprocally connected with M/T cells associated with other glomeruli. Reciprocal connectivity between M/T cells and GCs is defined as: M/T-1 excites GC-1 and GC-1 inhibits M/T-1, as observed by many studies [79,80]. Across the M/T population, there are 291 ± 9 (mean$\pm$SD, $n = 1250$ M/T cells) GCs that are reciprocally connected with each M/T cell. As a result, each PC projects to 7368 ± 64 GCs (mean$\pm$SD, $n = 10000$ PCs) with weight magnitude larger than 0.01. All feedback synaptic weights are randomly generated with small magnitude less than 0.05, and this structure gives rise to a dense but weak connectivity matrix $\mathbf{W}_{fb}$. Due to the sparsity of the PC firings when feedback is

ON, this dense and weak top-down connectivity ensures robust influence of PCs on GC activity and thus the contribution of PCx on odor processing in MOB.

Table 2 Network parameters controlling the connectivity between cell types.

	Connection density	**Average synaptic strength**	**References**
MCtoMC (same glomerulus)	0.8	0.25	2,81–83
MCtoMC (different glomeruli)*	0	0	
MC2GC	0.3	0.25	3,68,72,80
GC2MC	0.02	-0.4	
GC2GC	0.05	-0.1	68,84
MC2PC	0.5	0.06	4,6,22,85
MC2FFI	0.2	0.2	
PC2GC	0.9	0.03	86–88
PC2PC	0.01	0.1	22,71,89,90
FFI2PC	0.1	-0.1	
FBI2PC	0.8	-0.1	
FFI2FFI	0.01	-1.0	
PC2FBI	0.02	0.3	
FBI2FBI	0.02	-0.5	

*: We assumed zero connection between M/T cells associated with different glomeruli.

Model odor definition

Model odors are defined by the combinatorial patterns of glomeruli which are activated successively with different glomerular timing, a pattern recapitulating the spatiotemporal structure of odor inputs (Rubin and Katz, 1999; Meister and Bonhoeffer, 2001). Specifically, when a model odor is presented, 3~10 glomeruli will be activated ($6-20\%$ of all glomeruli) and all the M/T cells associated with those glomeruli will receive correlated glomerular input I^{osn} which lasts for 90ms. A table of 100 model odors were defined as the odor inputs to our network.

Modeling adult-neurogenesis as weight reshuffling

Adult-neurogenesis of the granule cells constantly removes old granule cells and replace them with adult-born ones. As a consequence, all the synapses from and onto old granule

cells are removed and new synapses with adult-born ones are built. We modeled this process by weight reshuffling in the network with the total number of granule cells fixed. On each simulation day, 10% of the granule cells had their synaptic weights reshuffled. For each granule cell, the values of synaptic weights changed randomly on each day. The distributions from which new synaptic weights were sampled from were the same distributions as building the network (see Table 3.2). We only reshuffled the individual weight values without changing the whole weight distributions.

Principal component analysis (PCA)

Spiking activity of each mitral/tufted cell and each piriform cell was binned into a $5ms$ sliding time window and averaged across trials (each model odor was presented in 10 trials). To perform the PCA analysis, we concatenated the trial-averaged responses of all mitral/tufted cells to all 100 model odors on all simulation days, resulting in a large matrix of 1250 cells by 247 time bins $\times$ 100 odors $\times$ 11 days. Response covariance matrices (1250 by 1250) were computed for this concatenated matrix (after subtracting the mean responses averaged across time bins, odors, and days). This gave us a single set of eigenvectors, thus the same eigenspace into which cell responses for all days can be projected and compared. Each 1250-dimensional cell response vector was then projected onto the first 3 principal eigenvectors for visualization and the first 50 principal eigenvectors for computations. The same procedure was also done for piriform cells.

Population vectors of firing rates and PCA trajectories

We constructed the population vectors using either the firing rates of all cells or the PCA trajectories of the first 50 dimensions. When using the firing rates, for each odor on each day, the single-trial responses all the cells was a matrix of 1250 cells by 247 time bins for M/T cells or $10{,}000$ cells by 247 time bins for piriform cells. We then converted the matrix into a long vector of lengths 1250×247 for M/T cells and $10{,}000 \times 247$ for piriform cells. When using PCA trajectories, the same procedures were applied, with only the cell number replaced by the reduced dimensionality.

Pairwise correlation between population vectors

To measure the similarity of population responses over time, we computed the Pearson's pairwise correlations of the population vectors constructed either by firing rates or PCA trajectories on two comparison days (for example, day-i and day-j). For within-odor correlation, the two population vectors were the responses (either single-trial or trial-averaged) to the same odor on day-i and day-j. For across-odor correlation, the two population vectors were the responses to any given two different odors on day-i and day-j, and we computed that for all different odor pairs on those two days. When $i = j$, the within-odor correlation was computed by comparing responses of even and odd trials.

Cosine similarity between population vectors

To gain a geometric perspective of the drift over days, we computed the cosine similarity of the population vectors by $\theta_{i,j} = \boldsymbol{u}_i \cdot \boldsymbol{u}_j / \|\boldsymbol{u}_i\| \times \|\boldsymbol{u}_j\|$, where $\theta_{i,j}$ is the cosine similarity between day-i and day-j, and $\boldsymbol{u}_i$ ($\boldsymbol{u}_j$) is the trial-averaged population vector on day-i (day-j). We also estimated the within-day variability for each odor on each day by computing the cosine similarity between the even trial-averaged and odd trial-averaged responses.

For within-day cosine similarity when $i = j$, we subtracted the estimated within-day variability from the computed cosine similarity.

Decoding analysis: K nearest neighbor algorithm

The K nearest neighbor approach was used to decode odor identity from the projected ensemble responses of PCs to any given odor pair [91]. Consistent with the computation of symmetrized Kullback–Leibler divergence D_{KL}, analysis was performed in the space of the first 50 principal components. The original data was broken up into testing and training sets. The training sets established the location of PC responses to known odors (i.e., known PC responses) in the principal component space and the testing sets were probed with respect to these known PC responses. The Euclidian distance of the unknown odors to all PC responses was then calculated and the K nearest neighbors were used to determine to which odor the unknown PC activity was responding to. This process of generating testing and training sets was repeated 30 times, with each repeat reflecting a different random population of testing and training to ensure that the decoding accuracy was not a result of artifacts of selecting a single testing/training population. Free parameters in the K nearest neighbor algorithm include the ratio of testing to training data, and the number of nearest neighbors used in the calculation. For training/testing, we used ratios of 50%, 70% and 90%. We also examined the algorithm's accuracy when 3, 5 and 7 nearest neighbors were used.

Spike-timing-dependent plasticity (STDP)

To model the effect of spike trains on synaptic weights, we used the suppression model given in [49]. Each pre- and post-synaptic spike was assigned with an efficacy $\epsilon_i = 1 - e^{-(t_i - t_{i-1})/\tau_s}$, where ϵ_i is the efficacy of the ith spike, t_i and t_{i-1} are the timing of the ith and $(i-1)$th spike respectively, and τ_s is the suppression time constant. The effect of each pair of pre- and post-synaptic spikes on synaptic modification was given by $\Delta w_{ij} = \epsilon_i^{pre} \epsilon_j^{pos} F(\Delta t_{ij})$, where ϵ_i^{pre} and ϵ_j^{pos} are the efficacies of the ith presynaptic spike and jth postsynaptic spike, respectively, and Δt_{ij} is the interval between the two spikes $t_j^{pos} - t_i^{pre}$. The function F represents the effect of temporal window for STDP, defined as:

$$F(\Delta t) \begin{cases} A_+ e^{-|\Delta t|/\tau_+} & if \quad \Delta t > 0 \\ A_- e^{-|\Delta t|/\tau_-} & if \quad \Delta t < 0 \end{cases} \tag{5}$$

Where A is the scaling factor, τ is the time constant, $+$ means long-term potentiation (LTP) and $-$ means long-term depression (LTD). We chose $\tau_s^{pre} = 34ms$, $\tau_s^{pos} = 75ms$. $A_{+/-}$ and $\tau_{+/-}$ are drawn from normal distributions for each synapse, where $A_+ \sim \mathcal{N}(1.03, 0.1)$, $A_- \sim \mathcal{N}(-0.51, 0.01)$, $\tau_+ \sim \mathcal{N}(13.3, 1.7)$ (in ms), $\tau_- \sim \mathcal{N}(34.5, 1.6)$ (in ms), and $\mathcal{N}(\mu, \sigma)$ represents normal distribution with mean μ and standard deviation σ.